Modelling of the Multi Jet Fusion Capillarity Effect on Close Facing Edges

Modelling of the Multi Jet Fusion Capillarity Effect on Close Facing Edges

Abstract

Purpose The objective of this research is to develop a physical model able to predict the shape of the capillarity effect in Multi Jet Fusion when two facing edges mutually affect each other. The work also aims at testing the consistency of such a model with experimental observations.

Design/methodology/approach

An analytical model of the phenomenon is developed considering the surface tension of the polymer melt adhering to the unfused powder. The general equilibrium equations are solved by imposing the boundary conditions corresponding to the case of two close facing edges, in which the shapes of the menisci are mutually influenced.

The analytical model is validated through an experimental activity. Specifically, a set of parallelepipeds with variable width was manufactured using an HP Multi Jet Fusion 4200. The morphologies of capillarities were captured via 3D scanning and compared with those predicted by the model.

Findings The results of this study demonstrate that the average error to the experimental capillarity profile is lower than that obtained by existing methods. Particularly, considerable improvements are achieved as far as the maximum capillarity height is concerned. The manufactured specimens exhibit a change in slope near the edges, which is arguably attributable to coating powder and other effects not included in the analytical model.

Originality/value The model presented in this study differs in hypotheses from previous methods in literature by assuming a null derivative of the capillarity shape in the central point of the meniscus. This allows for a more

accurate prediction of the defect morphology in the case of close facing edges.

Keywords: Additive Manufacturing, Multi Jet Fusion, Capillarity, Accuracy

1. Introduction

1.1. Motivation of the study

The central role of Additive Manufacturing (AM) in the future industry is nowadays well-established (Dilberoglu et al., 2017; Mehrpouya et al., 2019; Haleem and Javaid, 2019). AM technologies open a wide range of new opportunities thanks to their full digitalisation and the overcoming of several geometrical constraints of traditional manufacturing processes (Ngo et al., 2018; Ali et al., 2019). These aspects allow the development of groundbreaking business models (Savolainen and Collan, 2020). One of the most fascinating opportunities is mass customisation, i.e. the design and fabrication on a large scale of parts that are adapted to the needs of the individual customers (Deradjat and Minshall, 2017; Shukla et al., 2018).

One of the main limits to the economic sustainability of mass customisation is the generally low production rate of these technologies (Thomas and Gilbert, 2015; Gutowski et al., 2017). In fact, the high building time and the cost of the equipment have a major impact on the product cost (Costabile et al., 2016). Fig. 1 maps the production rate versus the resolution of different polymer-based AM processes (CIMdata Inc, 2018).

Fig. 1 shows that Multi Jet Fusion allows for achieving an impressive building rate. This feature, together with the mechanical properties of parts, makes the MJF extremely appealing for industrial applications of AM (O'Connor et al., 2018; Craft et al., 2018).

MJF is a powder-bed AM process patented by HP Inc. ®for transforming polymeric materials. Even though new materials have been recently introduced by HP, most of the applications are based on the use of PolyAmide (PA), sometimes reinforced with glass beads (O' Connor and Dowling, 2019).

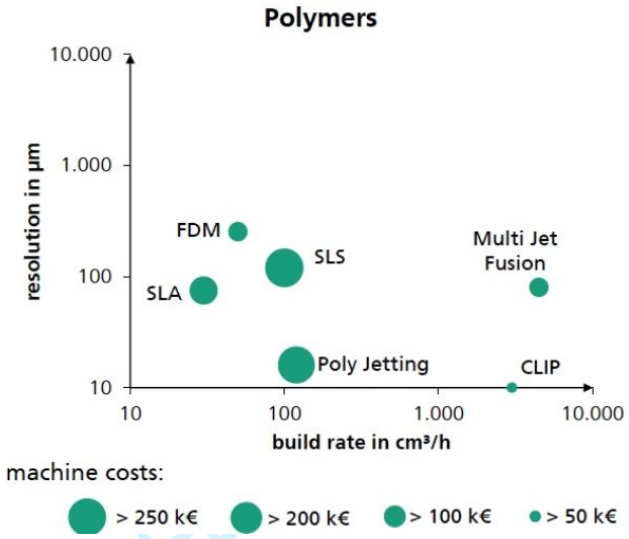

Figure 1: Comparison of Additive Manufacturing Technologies—Build Rate Compared to Resolution (Courtesy of Fraunhofer IAPT) (CIMdata Inc, 2018)

As in the High-Speed Sintering (HSS) process, a Fusing Agent (FA) is deposited through printheads on the powder bed (Thomas et al., 2006). The layer is then irradiated using an InfraRed Lamp (IRL), which melts the material wetted by Radiation Absorbing Material (RAM) (Ellis et al., 2014).

Unlike in HSS, a Detailing Agent (DA) is deposited at the borders of RAM. The DA prevents the undesired sintering of adjacent powder and the infiltration of molten material (Emamjomeh, AliPrasad et al., 2015). Fig. 2 shows a schematic representation of the process.

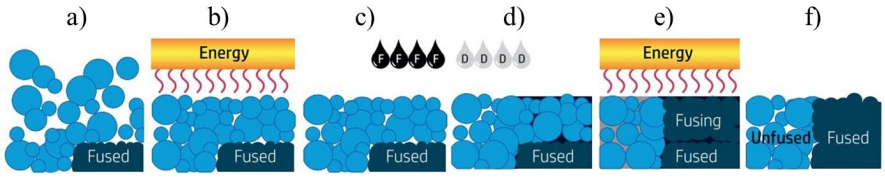

Figure 2: Scheme of the Multi Jet Fusion Process (adapted by HP Development Company L.P. (2014)). a) Material recoating, b) Thermal control, c) Application of the fusing agent, d) Application of the detailing energy, e) Fusion and f) Fused Layer.

Parts produced by MJF are characterised by almost isotropic mechanical behaviour and water tightness (Morales-Planas et al., 2018).

Despite the many benefits of this technology, MJF is characterised by some specific process-induced defects (HP Development Company L.P., 2017a). One of the most peculiar is the so-called capillarity effect, which is at the centre of this investigation.

1.2. Capillarity effect

As described in the previous section, two different agents are deposited on the layer, namely the FA and the DA. In order to prevent infiltration of molten polymer, the DA contains a surfactant, whose role is to limit the liquid material (Emamjomeh, AliPrasad et al., 2015). This surfactant increases the surface tension at the interface between the solid and the molten polymer, resulting in a local rise of the liquid meniscus (Rosen, 2012; De Gennes et al., 2013). Fig. 3 shows a detail of this phenomenon.

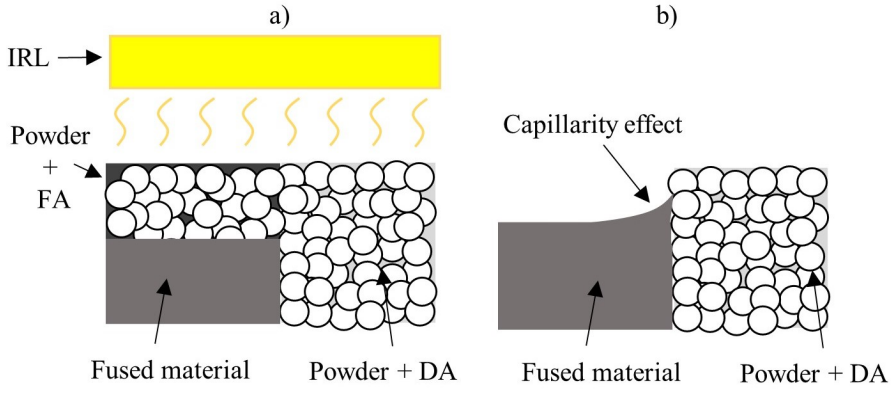

Figure 3: Scheme of the fusion process. a) InfraRed Lamp (IRL) melting powder soaked by Fusing Agent (FA). b) Fused material raising on powder soaked by Detailing Agent (DA).

After the solidification process is completed, the marker of the capillarity effect is still visible at the edges of the up-facing planes. Fig. 4 shows an example of this effect on a manufactured part.

A physical model of the capillarity is given by Mele et al. (2019). This model

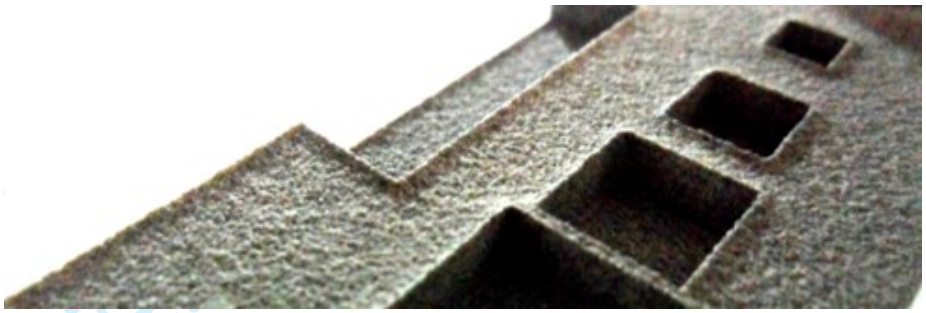

Figure 4: Picture of the capillarity effect on the manufactured part

assumes that this defect becomes null at an infinite distance to the edge, i.e. that the surface is sufficiently large to let the defect vanish away from borders. Such a condition is not met in the case of small parts with a small distance between facing edges. Therefore, in these cases, the model proposed by Mele et al. (2019) is not applicable.

A different solution of the physical model intended for application to cylindrical shapes was proposed by Mele et al. (2021). This model does not pose limitations in terms of dimensions but assumes that the surface where the capillarity effect arises is axisymmetric.

Therefore, these models do not allow for the prediction of the capillarity shape in the case of small surfaces with facing edges. To fill this gap, the present article derives a new equation to fit this case starting from a physical model of the process. A benchmark part is then designed and manufactured to observe the actual shape of the defect. The profile of the capillarity effect is acquired through 3D scanning and compared to the analytical results to validate the model.

2. Analytical model

For the scope of this study, it is assumed that the molten polymer in contact with the unmelted powder infiltrated by DA behaves like a liquid facing a vertical solid wall. Such an assumption is common to previous literature on the

capillarity effect in MJF (Mele et al., 2019, 2021).

The interfacial tension γ between the solid and the liquid is a characteristic value given a certain combination of materials (De Gennes et al., 2013). Also, the interface is characterised by the contact angle θ_e between the two phases.

This study investigates the case of two vertical walls facing each other. As a hypothesis, the two edges are assumed to be parallel and their normal direction is referred to as **x**. The analysed system is represented in Fig. 5, in which b indicates the half distance between the edges along the **x**-axis and θ_e is the contact angle between the liquid and solid phases. As can be seen, the coordinate system is located in the central point of the meniscus. Fig. 5 highlights also an element of infinitesimal length dx (coloured in red). Fig. 6 shows a detail of this element.

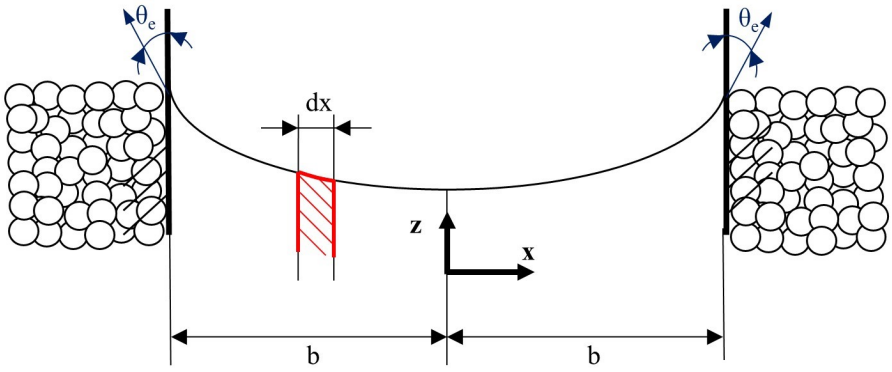

Figure 5: Model of the meniscus between two facing edges and infinitesimal element of length dx (red coloured).

Fig. 6 shows that the infinitesimal element is subject to the hydrostatic force F_{hs}, directed along the negative **z** direction. The module of this force can be calculated as in Eq. 1:

$$F_{hs} = \rho \times g \times z \times dx \tag{1}$$

where ρ is the density of the liquid, g is the acceleration of gravity, z is the local height of the meniscus and dx is the infinitesimal length along the **x**-axis.

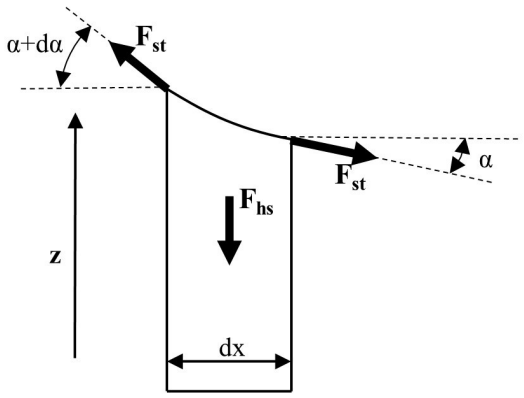

Figure 6: Detail of an infinitesimal element dx

As shown in Fig. 6, the element is also subject to the force F_{st} due to the interfacial tension γ mentioned above.

This force is tangent to the meniscus. The inclinations of F_{st} at the right and left side of the infinitesimal element are indicated as α and $\alpha + d\alpha$, respectively. Assuming a unitary depth of the infinitesimal element, the modulus of F_{st} is equal to the surface tension γ.

Under these assumptions, Eq. 2 expresses the condition of vertical equilibrium on the infinitesimal element:

$$\Delta\rho \times g \times z \times dx = \gamma \times sin(\alpha + d\alpha) - \gamma \times sin(\alpha) \cong \gamma \times \cos(\alpha) \times d\alpha \qquad (2)$$

It is worth noticing that the density ρ in Eq. 1 has been replaced with the term $\Delta\rho$, which represents the difference in density between the powder and the molten polymer. The aim is to consider the powder coating effect on the meniscus.

According to the representation in Fig. 6, the tangent of the angle α is given in Eq. 3:

$$tan(\alpha) = \frac{dz}{dx} \qquad (3)$$

where dx and dz are the infinitesimal increments along the x and z-axes, respectively.

Under these assumptions, the condition of equilibrium leads to Eq. 4 (Mele et al., 2019):

$$z(x) = \frac{\gamma}{\triangle\rho \times g} \times \frac{d^2z}{dx^2} = k^{-2}\frac{d^2z}{dx^2} \tag{4}$$

Where k^-1 is the characteristic length of the capillary, defined as in Eq. 5) (De Gennes et al., 2013):

$$k^{-1} = \sqrt{\frac{\gamma}{\Delta\rho \times g}} \tag{5}$$

To solve the differential equation in Eq. 4, it is necessary to introduce the boundary conditions of the problem. As stated above, the contact angle θ_e between the solid and the liquid is a characteristic of the pair of materials. This condition is expressed in Eq. 6:

$$\frac{dz}{dx}_{x=b} = cot(\theta_e) \tag{6}$$

The second hypothesis is that the shape of the meniscus is symmetric, i.e. the direction of the defect has no influence on the capillarity effect. Under this assumption, the slope of the meniscus is null on the centre point of the two walls, as expressed in Eq. 7:

$$\frac{dz}{dx}_{x=0} = 0 \tag{7}$$

Solving Eq. 4 with the boundary conditions in Eq. 6 and Eq. 7 leads to the result in Eq. 8, which describes the profile of the surface between the two edges.

$$z(x,b) = \frac{e^{k(b-x)}(1+e^{2k\,x})k^{-1}cot(\theta_e)}{e^{2k\,b}-1} \tag{8}$$

The model in Eq. 8 will be referenced in the following as Close Edges Capillarity Model (CECM). This model can also be used to calculate the value of the meniscus rise in the central point, i.e. at x=0, as shown in Eq. 9:

$$z(0,b) = \frac{2e^{kb}}{e^{2k\,b} - 1} k^{-1} cot(\theta_e) \tag{9}$$

It can be observed that the value in Eq. 9 asymptotically tends to 0 when b approaches infinity, i.e. $\lim_{b\to\infty} z(0,b) = 0$. Even though this value is never reached, the height of the central point becomes negligible above a certain width b which depends on the values of θ_e and k^{-1}. This criterion can be applied to determine the distance at which the edges can be considered close. A practical example is given in the next section when defining the dimensions of specimens.

To calculate the maximum rise of the liquid, Eq. 8 is computed at x=b, as shown in Eq. 10:

$$z(b,b) = \frac{e^{2kb} + 1}{e^{2k\,b} - 1} k^{-1} cot(\theta_e) \tag{10}$$

To calculate the maximum height of the capillarity z_{max}, the difference between the maximum and minimum rise of the liquid, i.e. between Eq. 10 and Eq. 9, must be calculated. This leads to the result in Eq. 11:

$$z_{max}(b) = z(b,b) - z(0,b) = k^{-1} cot(\theta_e) tanh(\frac{kb}{2}) \tag{11}$$

The expression in Eq. 11 tends to 0 when b approaches 0, i.e. $\lim_{b\to 0} z_{max}(b) = 0$. In fact, when reducing the distance to edges, the effect of the force F_{st} due to interfacial tension is dominant also in the central region, whose difference with edges vanishes. In these conditions, the meniscus tends to have a flat shape. It is worth mentioning that both Eq. 9 and 10 tend to infinity when b approaches 0 since the interfacial tension becomes dominant on gravity and the liquid moves upward under the effect of capillarity. In the MJF process, the rise is limited by the height of the deposited powder layer, as shown in Fig. 3.

Observing Eq. 11, it is also possible to notice that, as b approaches infinity, the maximum height tends to the finite value in Eq. 12:

$$\lim_{b\to\infty} z_{max}(b) = k^{-1} cot(\theta_e). \tag{12}$$

Eq. 8 can be reformulated by moving the origin of the x-axis on the left edge of the capillarity by substituting x with $x - b$. Operating this substitution and calculating the limit as b approaches infinity leads to the result shown in Eq. 13, which is the theoretical upper limit to the capillarity height.

$$\lim_{b \to \infty} \frac{e^{k(2b-x)}(1 + e^{2k(x-b)})k^{-1}cot(\theta_e)}{e^{2k\,b} - 1} = e^{-kx}k^{-1}cot(\theta_e) \tag{13}$$

The right side of Eq. 13 is the model of capillarity obtained by Mele et al. (2019), which will be referenced as *Free Edge Capillarity Model (FECM)* in the following. This is consistent with the physics of the problem, since increasing b the mutual influence of the two edges vanishes and the FECM can be applied.

3. Experimental activity

3.1. Design and manufacturing of specimens

The benchmark in Fig. 7 has been designed to inspect the capillarity effect between facing edges. The coordinate system in Fig. 7 shows the orientation of the part within the build chamber. As can be observed, the benchmark comprises five planar top surfaces where the capillarity effect is observed. It is worth underlining that the five repetitions of each test condition are carried out on the same benchmark. This allows for minimising the effect of process conditions, e.g. part cooling, which can alter the final result (Mele et al., 2020b). On the other hand, this approach may suffer from limitations whether an external factor affects the quality of the entire manufactured part. This risk is accepted as this study focuses on a local effect, namely capillarity, which is unlikely to be systematically altered in all the regions of the part by external factors. Further applications of the method will be necessary to test its consistency in different processing conditions.

The thickness of the part is limited to prevent sinking, which may alter the observation (HP Development Company L.P., 2017b). Observing Fig. 7 it is possible to notice that the only variable dimension is the width of the upper planes, namely the faces where the capillarity effect is measured.

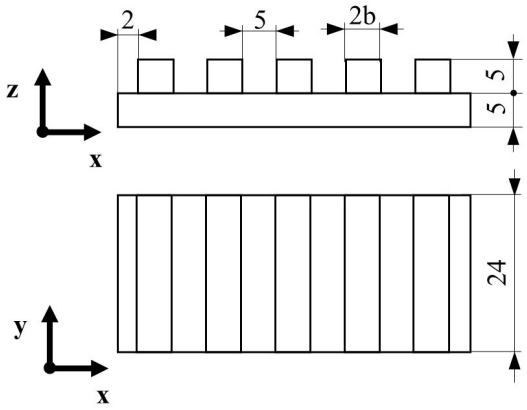

Figure 7: Benchmark used to observe the capillarity effect (dimensions in mm)

All the specimens were produced through an HP MJF 4200 using PA12 powder, the properties of which are summarised in Tab. 1.

Table 1: Properties of the PA12 powder used for testing

Property	Value	Reference
Particle size (μm)	60	(Morales-Planas et al., 2018)
Powder Bulk density ($\frac{g}{cm^3}$)	0.425	(Morales-Planas et al., 2018)
Onset melting temperature ($°C$)	180.5	(Sillani et al., 2019)
First melting fusion enthalpy ($J\,g^{-1}$)	110.3	(Sillani et al., 2019)
Cristallinity (%)	52.7	(Sillani et al., 2019)
Crystallization temperature ($°C$)	148.6	(Sillani et al., 2019)
Crystallization enthalpy ($J\,g^{-1}$)	47.9	(Sillani et al., 2019)
Moleculare weigth (M_N) ($\frac{g}{mol}$)	80,852	(Sillani et al., 2019)
Moleculare weigth (M_W) ($\frac{g}{mol}$)	41,020	(Sillani et al., 2019)
Polydispersity (-)	1.97	(Sillani et al., 2019)

The irradiance of the machine was set to -3.5% after the fine-tuning procedure. The fast printing mode was used for the process (HP Development Company L.P., 2014). The room where the production took place was maintained at $25 \pm 5°C$ temperature and humidity $40 \pm 5\%$. The main process parameters

are summarised in Tab. 2 (Mele et al., 2019).

Table 2: Parameters of the MJF process (Mele et al., 2019)

Property	Value
Layer build time (s)	7.6
Fusing agent ($\frac{mm^3}{mm^3(part)}$)	58×10^{-3}
Detailing agent ($\frac{mm^3}{mm^3(part)}$)	62×10^{-3}

The benchmarks were positioned in the bottom central region of the build volume. The build job included 45 parts with a total volume of 28,052.57 mm^3. The total build height and nesting density were equal to 112.13 mm and 6.23%, respectively.

As shown in Fig. 7, the profile is oriented along the x-axis. the average values observed on the west and east edges by Mele et al. (2019) are used to calculate the profile in Eq. 8. These values are summarised in Tab. 3

Table 3: Parameters used for calculation of Eq. 8 (Mele et al., 2019)

Property	Value
k^{-1} (mm)	1.545
θ_e (°)	78.3
γ ($\frac{mN}{m}$)	15.91
$\Delta\rho$ ($\frac{kg}{m^3}$)	675

Entering values of Tab. 3 in Eq. 9, it can be verified that the value of z(0,b) decreases below 0.01 mm when b exceeds 5.36 mm. This is thus considered an upper limit to define close edges in the investigated case. Accordingly, four different specimens were designed varying the values of b from 2 to 5 mm with a step of 1 mm.

After unpacking, the parts were manually brushed to prevent accidental modifications of the capillary effect during air blasting.

3.2. Measurement of the capillarity effect

In order to observe the shape of the top surfaces, all the specimens were digitalised by means of a FARO ScanArm non-contact structured blue light 3D scanner. The software Geomagic® Control X™by 3D System © was used to manage the acquired scans. Particularly, the clouds of points captured through the scanner were aligned to the digital models of benchmarks using the best-fit option provided by the software. The distance between the model and the point cloud was measured along parallel lines directed as the **x**-axis, as shown in Fig. 8.

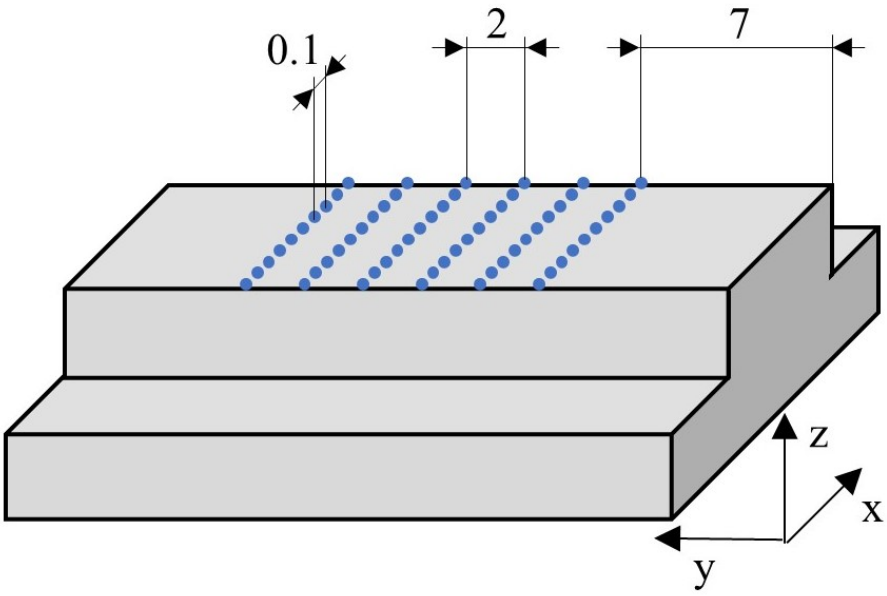

Figure 8: Scheme of comparison points on upper surfaces

A distance of 7 mm is kept between these lines and the sides of the specimen, so as to avoid the influence of border edges. Six parallel lines with step 2 mm along the **y**-axis are analysed for each surface, resulting in 30 measuring lines per specimen.

For each line, the distance along **the z-axis** between the point cloud and the CAD model is measured in fixed positions (represented as blue dots in Fig. 8)

by using the comparison point tool of Geomagic® Control X™. The comparison points are located at $\Delta r = 0.1mm$ one from each other starting from the edge, as shown in Fig. 8. The total number of comparison points along a scanning line (N_p) can be thus calculated as in Eq. 14:

$$N_p = (\frac{2b}{\Delta r} + 1) \tag{14}$$

Tab. 4 summarises the measures and comparison points of each specimen.

Table 4: Widths and comparison points of the different specimens

Specimen	b (mm)	N_p	Total comparison points
1	5	101	606
2	4	81	486
3	3	61	366
4	2	41	246

As can be seen in Tab. 4, a minimum of 246 sample points is tested on the smallest benchmark, i.e. when b=2 mm.

The distances between the scan and the CAD model at comparison points were exported by Geomagic® Control X™as plain text files. These files were then imported to Microsoft® Excel™to perform the data analysis detailed in the following.

As described by Attene et al. (2003), the contactless measuring system causes chamfering of sharp edges. For this reason, the very last point of each measuring line is excluded from the analysis.

For each upper plane j, the average height $\bar{z}_j(x)$ at the generic coordinate x is calculated as the average value measured on the six measuring lines.

The measured profile $\bar{z}(x)$ on the specimen is then obtained as the average of $\bar{z}_j(x)$ on the five planes, i.e. as in Eq. 15:

$$\bar{z}(x) = \frac{\sum_{j=1}^{5} \bar{z}_j(x)}{5} = \frac{1}{5}\sum_{j=1}^{5}(\frac{1}{6}\sum_{j=1}^{6}\bar{z}_{i,j}(x)) \tag{15}$$

where $\bar{z}_{i,j}(x)$ is the height measured at position x along the i-th of the six measuring lines on the j-th top plane. Using the same notation, the standard deviation of measurements at the position x is calculated as in Eq. 16:

$$\sigma_z(x) = \sqrt{\frac{1}{4}\sum_{j=1}^{5}(\bar{z}(x) - \bar{z}_j(x))^2} \tag{16}$$

The average value of standard deviation on the profile of semi-width b ($\bar{\sigma}(b)$) can be calculated as in Eq. 17. $\bar{\sigma}(b)$ provides an estimation of the consistency of the capillarity profile among the measuring lines. This information is used to verify whether the number of repetitions, i.e. 30 lines per each of the four values of b, is sufficient to reliably represent the defect.

$$\bar{\sigma}(b) = \frac{1}{N_p}\sum_{k=0}^{N_p-1}\sigma_z(k \times \Delta r) \tag{17}$$

3.3. Error between prediction and calculation

The error of the prediction is calculated as the absolute value of the difference between $z(x)$ (Eq. 8) and $\bar{z}(x)$ (Eq. 15).

The overall per cent average error of the prediction $\bar{E}(b)$ is calculated in Eq. 18, while the corresponding standard deviation σ_E is given in Eq. 19. These values will be used in the next section to describe the accuracy of the model.

$$\bar{E}(b) = \frac{1}{N_p}\sum_{k=0}^{N_p-1}\frac{\bar{z}(k \times \Delta r) - z(k \times \Delta r)}{\bar{z}(k \times \Delta r)} \tag{18}$$

$$\sigma_E = \sqrt{\frac{1}{N_p - 1}\sum_{k=0}^{N_p-1}(\bar{E} - \frac{\bar{z}(k \times \Delta r) - z(k \times \Delta r)}{\bar{z}(k \times \Delta r)})^2} \tag{19}$$

3.4. Results and discussion

Tab. 5 shows the average values of standard deviation $\bar{\sigma}(b)(mm)$ on the profiles. It is possible to notice that these values are below 20 μm on each specimen. This finding demonstrates that the shape of the capillarity effect is consistent among the 30 measurement lines of each specimen. This suggests

that the number of repetitions, i.e. 5 planes per part and 6 measuring lines on each plane, is sufficient to achieve a reliable representation of the defect. Therefore, it is possible to use the average profile $\bar{z}(x)$ as a reliable estimation of the planar top surfaces for a given semi-width b.

Table 5: Average values of standard deviation

Specimen	b (mm)	$\bar{\sigma}$ (mm)
1	5	0.005
2	4	0.013
3	3	0.016
4	2	0.017

Tab. 6 summarises the per cent average error between the predicted and measured profile ($\bar{E}$) and the corresponding standard deviation (σ_E). The average percent error of the FECM is also reported for comparison.

Table 6: Error between calculated and measured profile of the capillarity effect

Specimen	b (mm)	$\bar{E} \pm \sigma_E\,(CECM)$ (%)	$\bar{E} \pm \sigma_E\,(FECM)$ (%)
1	5	-15.3 ± 27.7	29.3 ± 36.7
2	4	-23.7 ± 22.4	47.1 ± 128.3
3	3	-31.6 ± 25	35.2 ± 67.8
4	2	-30.0 ± 40.9	66.1 ± 82.7

Results in Tab. 6 show that the CECM leads to negative values of $\bar{E}$, i.e. the model averagely underestimates the measured shapes. On the contrary, a positive error is obtained by FECM. The absolute value of $\bar{E}$ is always lower in the case of CECM. This finding demonstrates that the model proposed in this study allows for a more accurate estimation of the capillarity shape if compared with existing methods.

The underestimation of the profile provided by CECM may be critical in case this model is integrated with redesign strategies aiming at removing the

capillarity effect, such as that proposed by Mele et al. (2020a). Also, in this case, several design iterations should be performed updating the distance b between edges.

High values of standard deviation σ_E are found in all the observations. The reason for this is that the distance between the prediction and the measurement is unevenly distributed along the x-axis. This can also be seen in Figs. 9 - 12, which show the comparison between the calculated and measured profiles of the capillarity effect, namely $z(x)$ and $\bar{z}(x)$, respectively.

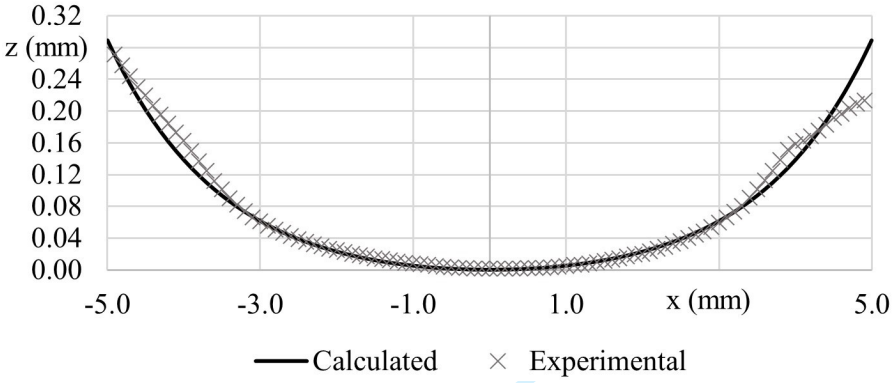

Figure 9: Comparison between z(x) and $\bar{z}(x)$ for specimen 1 (b= 5 mm)

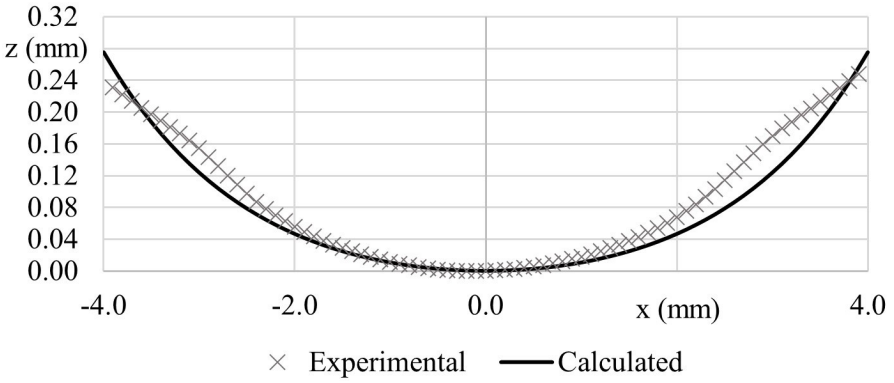

Figure 10: Comparison between z(x) and $\bar{z}(x)$ for specimen 2 (b= 4 mm)

The overlap of the curves shows that the measured profiles present an in-

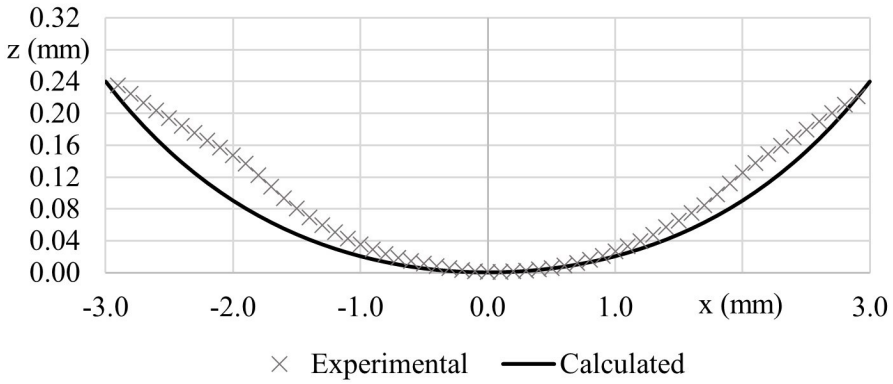

Figure 11: Comparison between z(x) and $\bar{z}(x)$ for specimen 3 (b= 3 mm)

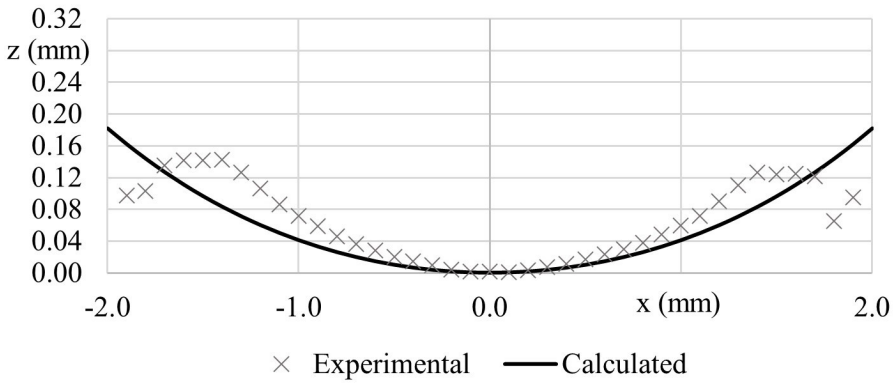

Figure 12: Comparison between z(x) and $\bar{z}(x)$ for specimen 4 (b= 2 mm)

flexion that is not calculated by Eq. 8. This difference is arguably attributable to other influential factors which are not considered by the model, such as the covering powder and the coating detailing agent. The present model does not allow for directly including these factors since, as discussed in Section 2, it starts from the assumption that the polymer melt behaves like a liquid facing a solid wall. Future research will be dedicated to understanding if this gap between analytical and experimental results can be filled through empirical factors or changing the hypotheses of the physical model.

It is worth mentioning that the average error presented in Tab. 6 is subject

to variations due to the accuracy of the measuring system. In fact, in the central region of the profile the values of $\bar{z}(x)$ are in the same order of magnitude as the accuracy of the measuring system. Further analysis is thus performed comparing the maximum measured height of the capillarity ($\bar{z}_{max}$) with that calculated by the model (z_{max}). Fig. 13 shows this comparison for both CECM and FECM. The per cent errors ($\bar{E}_{zmax}$) of the two models are summarised in Tab. 7.

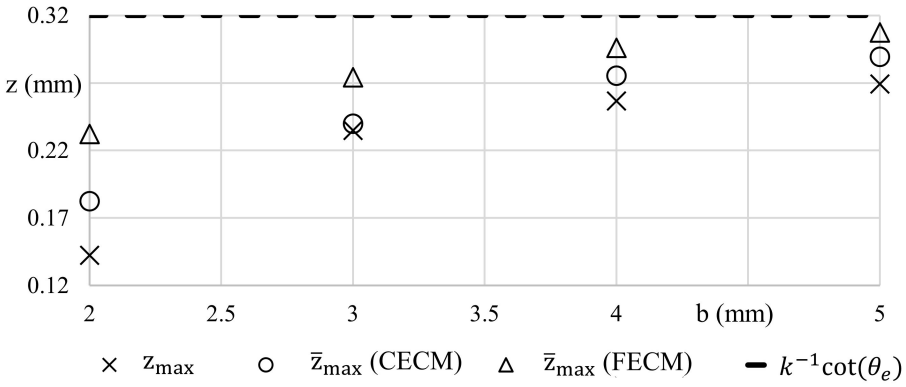

Figure 13: Maximum capillarity height as a function of the part width

Table 7: Error between the calculated and measured profile of the capillarity effect

Specimen	b (mm)	$\bar{z}_{max}$ (μm)	$\bar{E}_{zmax},(CECM)$ (%)	$\bar{E}_{zmax},(FECM)$ (%)
1	5	142	7.5	14.2
2	4	235	7.2	15.3
3	3	257	2.1	16.8
4	2	269	28.1	63.2

Results in Fig. 13 and Tab. 7 show that the maximum height of the capillarity increases while b increases, plateauing below the maximum theoretical value $k^{-1}cot(\theta_e)$ (which is equal to 0.32 mm). These experimental observations are consistent with the physical model of the phenomenon discussed in Section 2.

The error values in Tab. 7 demonstrate that the CECM allows for a substantially better estimation of $\bar{z}_{max}$ if compared with FECM, especially for low values of b. The graphical representation in Fig. 13 shows that the predictions of FECM and CECM tend to converge while increasing b. This result is expected since, as discussed in Section 2, CECM approaches FECM as the mutual influence of facing edges decreases.

4. Conclusions

The CECM presented in this study allows for a more accurate estimation of the capillarity shape on close facing edges by MJF if compared with existing models. Particularly, findings demonstrate a considerable reduction of the average per cent error between the calculated and measured capillarity profile. Unlike in the case of FECM, the CECM leads to negative errors, i.e. an average underestimation of the real shape is obtained.

The advantages of CECM over FECM are evident also as far as the maximum height of the capillarity is concerned. Particularly, the estimation obtained through the newly proposed model is highly more realistic for the smallest measured observed. While increasing the distance between edges, results of FECM and CECM approach each other.

The comparison between calculated and experimental curves shows an inflexion of the actual capillarity shape, which is not predicted by CECM. This effect is arguably attributable to influential factors not represented by the **physical** model and deserves further research to be unveiled.

Acknowledgements

The authors would like to thank the MIUR (Italian Ministry of University and Research) for funding support and Juno Design S.r.l. for laboratory facilities.

References

Ali, M.H., Batai, S., Sarbassov, D., 2019. 3D printing: a critical review of current development and future prospects. Rapid Prototyping Journal 25, 1108–1126. doi:10.1108/RPJ-11-2018-0293.

Attene, M., Falcidieno, B., Rossignac, J., Spagnuolo, M., 2003. Edge-sharpener: recovering sharp features in triangulations of non-adaptively re-meshed surfaces. Proceedings of the 2003 Eurographics/ACM SIGGRAPH symposium on Geometry processing , 62–69URL: http://dl.acm.org/citation.cfm?id=882378.

CIMdata Inc, 2018. Industrialization of Additive Manufacturing Accessible Today. Technical Report July.

Costabile, G., Fera, M., Fruggiero, F., Lambiase, A., Pham, D., 2016. Cost models of additive manufacturing: A literature review. International Journal of Industrial Engineering Computations 8, 263–282. doi:10.5267/j.ijiec.2016.9.001.

Craft, G., Nussbaum, J., Crane, N., Harmon, J.P., 2018. Impact of extended sintering times on mechanical properties in PA-12 parts produced by powderbed fusion processes. Additive Manufacturing 22, 800–806. URL: https://doi.org/10.1016/j.addma.2018.06.028, doi:10.1016/j.addma.2018.06.028.

De Gennes, P.G., Brochard-Wyart, F., Quéré, D., 2013. Capillarity and wetting phenomena: drops, bubbles, pearls, waves. Springer Science & Business Media.

Deradjat, D., Minshall, T., 2017. Implementation of rapid manufacturing for mass customisation. Journal of Manufacturing Technology Management 28, 95–121. doi:10.1108/JMTM-01-2016-0007.

Dilberoglu, U.M., Gharehpapagh, B., Yaman, U., Dolen, M., 2017. The Role of Additive Manufacturing in the Era of Industry 4.0. Procedia Manufacturing

11, 545–554. URL: http://dx.doi.org/10.1016/j.promfg.2017.07.148, doi:10.1016/j.promfg.2017.07.148.

Ellis, A., Noble, C.J., Hopkinson, N., 2014. High Speed Sintering: Assessing the influence of print density on microstructure and mechanical properties of nylon parts. Additive Manufacturing 1, 48–51. URL: http://dx.doi.org/10.1016/j.addma.2014.07.003, doi:10.1016/j.addma.2014.07.003.

Emamjomeh, AliPrasad, K.A., Novick, M.A., Fung, E.M., 2015. Detailing agent for three-dimensional (3d) printing.

Gutowski, T., Jiang, S., Cooper, D., Corman, G., Hausmann, M., Manson, J.A., Schudeleit, T., Wegener, K., Sabelle, M., Ramos-Grez, J., Sekulic, D.P., 2017. Note on the Rate and Energy Efficiency Limits for Additive Manufacturing. Journal of Industrial Ecology 21, S69–S79. doi:10.1111/jiec.12664.

Haleem, A., Javaid, M., 2019. Additive Manufacturing Applications in Industry 4.0: A Review. Journal of Industrial Integration and Management 04, 1930001. doi:10.1142/s2424862219300011.

HP Development Company L.P., 2014. HP Multi Jet Fusion technology. Technical White Paper , 8.

HP Development Company L.P., 2017a. Multi Jet Fusion printing tips and tricks. Technical White Paper .

HP Development Company L.P., 2017b. Multi Jet Fusion printing tips and tricks. Technical White Paper .

Mehrpouya, M., Dehghanghadikolaei, A., Fotovvati, B., Vosooghnia, A., Emamian, S.S., Gisario, A., 2019. The Potential of Additive Manufacturing in the Smart Factory Industrial 4.0: A Review. Applied Science , 34.

Mele, M., Campana, G., Monti, G.L., 2019. Modelling of the capillarity effect in Multi Jet Fusion technology. Additive Manufacturing

30, 100879. URL: https://linkinghub.elsevier.com/retrieve/pii/S2214860419305664, doi:10.1016/j.addma.2019.100879.

Mele, M., Campana, G., Monti, G.L., 2020a. A finned-riser design to avoid the capillarity effect in multi-jet fusion technology. Rapid Prototyping Journal doi:10.1108/RPJ-01-2020-0020.

Mele, M., Campana, G., Monti, G.L., 2021. Modelling of the capillarity effect for cylindrical shapes in Multi Jet Fusion technology. Progress in Additive Manufacturing URL: https://doi.org//10.1007/s40964-021-00200-7, doi:10.1007/s40964-021-00200-7.

Mele, M., Campana, G., Pisaneschi, G., Monti, G.L., 2020b. Investigation into effects of cooling rate on properties of polyamide 12 parts in the multi jet fusion process. Rapid Prototyping Journal 26, 1789–1795. doi:10.1108/RPJ-04-2020-0080.

Morales-Planas, S., Minguella-Canela, J., Lluma-Fuentes, J., Travieso-Rodriguez, J.A., García-Granada, A.A., 2018. Multi Jet Fusion PA12 manufacturing parameters for watertightness, strength and tolerances. Materials 11, 1–11. doi:10.3390/ma11081472.

Ngo, T.D., Kashani, A., Imbalzano, G., Nguyen, K.T., Hui, D., 2018. Additive manufacturing (3D printing): A review of materials, methods, applications and challenges. Composites Part B: Engineering 143, 172–196. URL: https://doi.org/10.1016/j.compositesb.2018.02.012, doi:10.1016/j.compositesb.2018.02.012.

O' Connor, H.J., Dowling, D.P., 2019. Comparison between the properties of polyamide 12 and glass bead filled polyamide 12 using the multi jet fusion printing process. Additive Manufacturing 31, 100961. URL: https://linkinghub.elsevier.com/retrieve/pii/S2214860419300958, doi:10.1016/j.addma.2019.100961.

O'Connor, H.J., Dickson, A.N., Dowling, D.P., 2018. Evaluation of the mechanical performance of polymer parts fabricated using a production scale multi jet fusion printing process. Additive Manufacturing 22, 381–387. doi:10.1016/j.addma.2018.05.035.

Rosen, M., 2012. Surfactants and interfacial phenomena. volume 40. doi:10.1016/0166-6622(89)80030-7.

Savolainen, J., Collan, M., 2020. How Additive Manufacturing Technology Changes Business Models? – Review of Literature. Additive Manufacturing 32, 101070. URL: https://doi.org/10.1016/j.addma.2020.101070, doi:10.1016/j.addma.2020.101070.

Shukla, M., Todorov, I., Kapletiac, D., 2018. Application of Additive Manufacturing for Mass Customization: Understanding the Interaction of Critical Barriers. Production Planning & Control 29, 814–825.

Sillani, F., Kleijnen, R.G., Vetterli, M., Schmid, M., Wegener, K., 2019. Selective laser sintering and multi jet fusion: Process-induced modification of the raw materials and analyses of parts performance. Additive Manufacturing 27, 32–41. URL: https://doi.org/10.1016/j.addma.2019.02.004, doi:10.1016/j.addma.2019.02.004.

Thomas, D.S., Gilbert, S.W., 2015. Costs and cost effectiveness of additive manufacturing: A literature review and discussion. Additive Manufacturing: Costs, Cost Effectiveness and Industry Economics , 1–96.

Thomas, H.R., Hopkinson, N., Erasenthiran, P., 2006. High Speed Sintering – Continuing Research into a New Rapid Manufacturing Process. Proceedings of the 17th Solid Freeform Fabrication Symposium (SFF) , 682–691URL: http://sffsymposium.engr.utexas.edu/2006TOC%0Ahttp://sffsymposium.engr.utexas.edu/Manuscripts/2006/2006-59-Thomas.pdf.

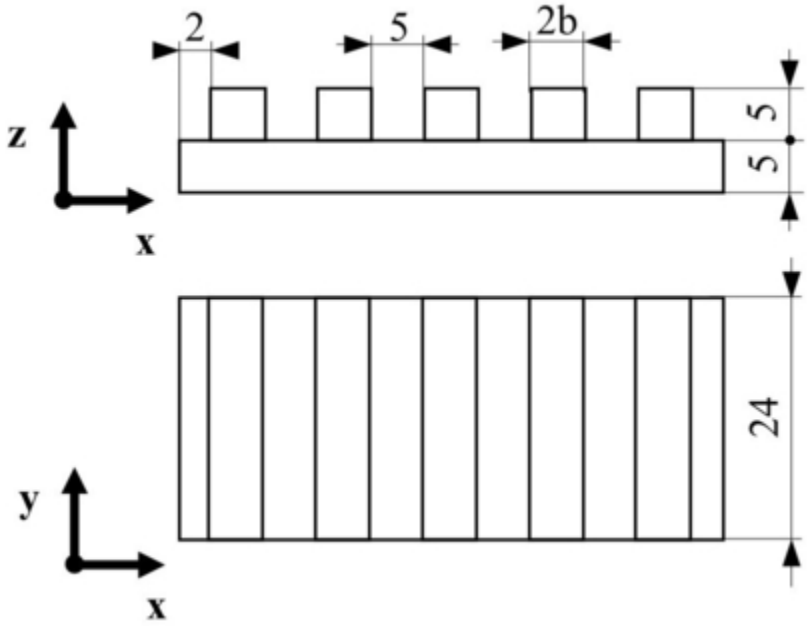

71x56mm (150 x 150 DPI)

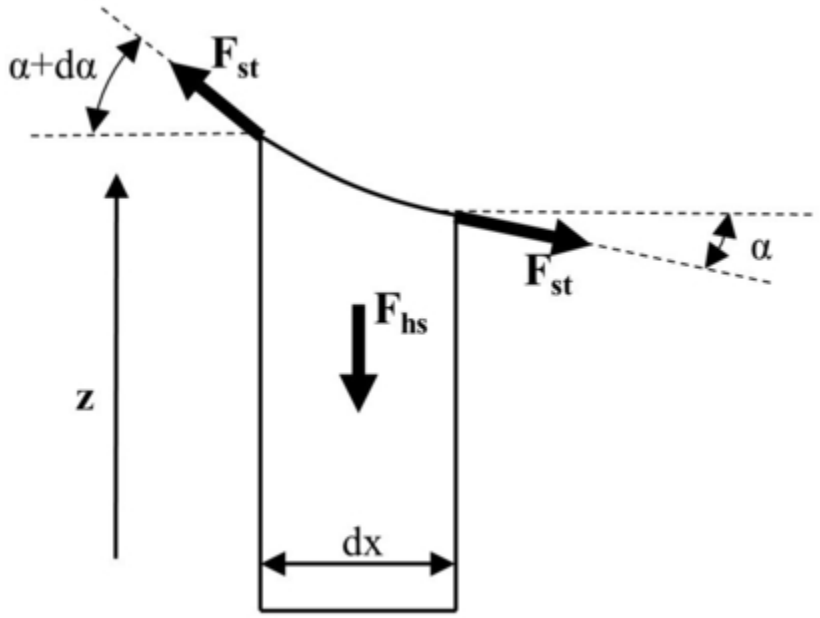

73x54mm (150 x 150 DPI)

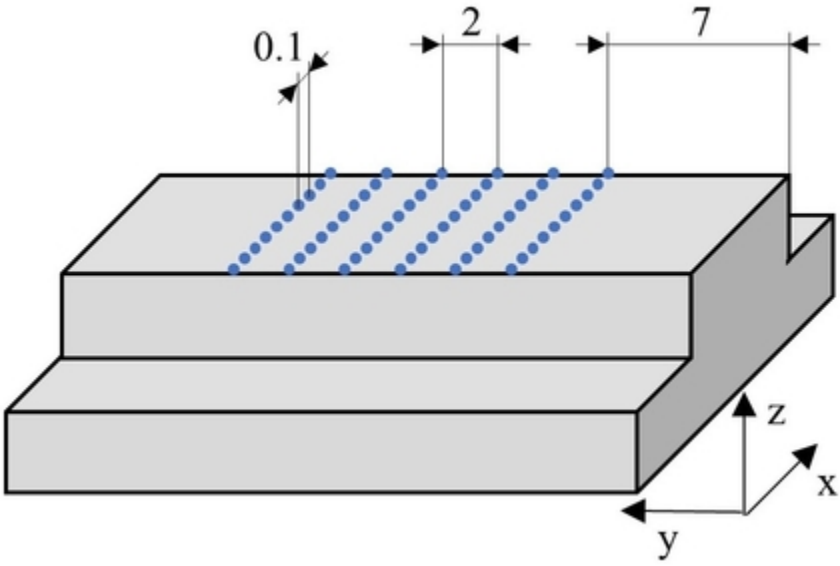

73x49mm (150 x 150 DPI)

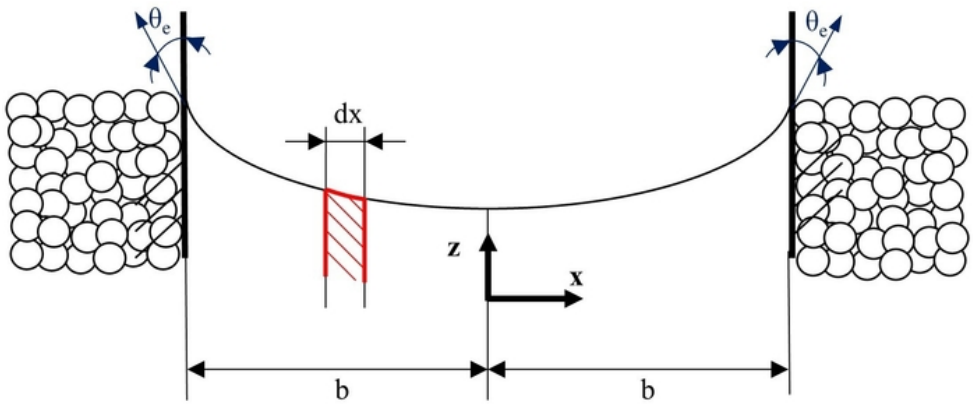

121x52mm (150 x 150 DPI)

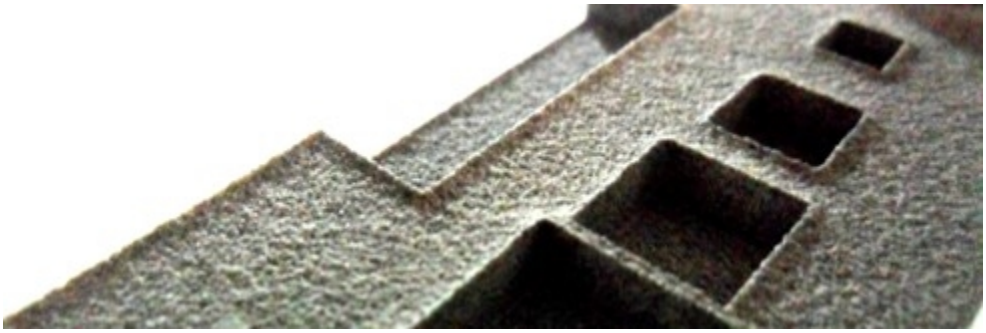

82x27mm (150 x 150 DPI)

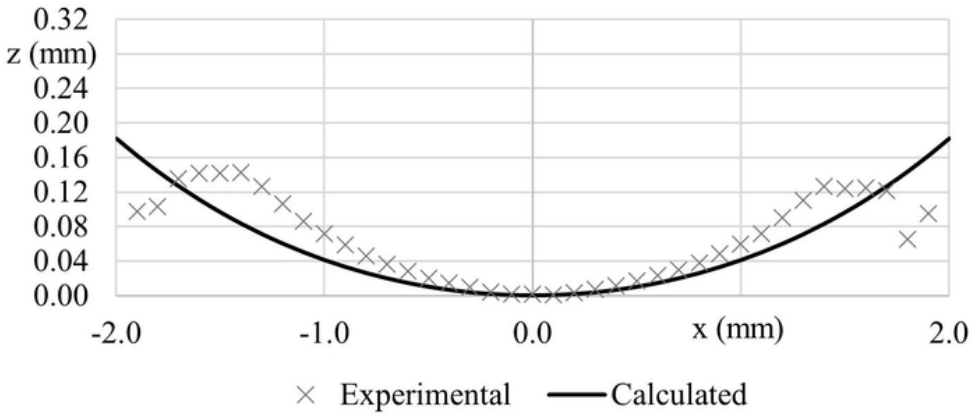

121x53mm (150 x 150 DPI)

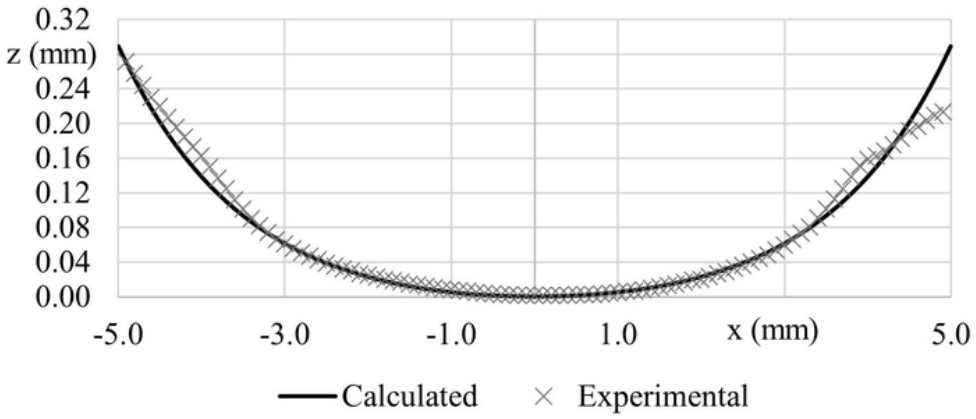

121x52mm (150 x 150 DPI)

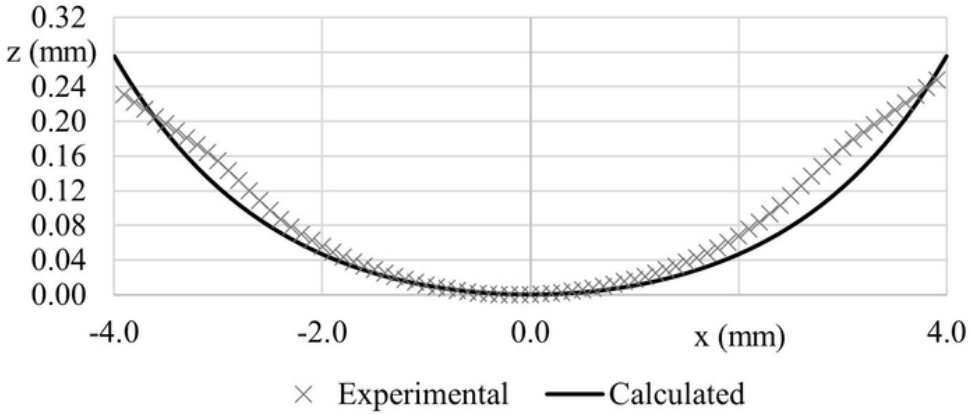

121x52mm (150 x 150 DPI)

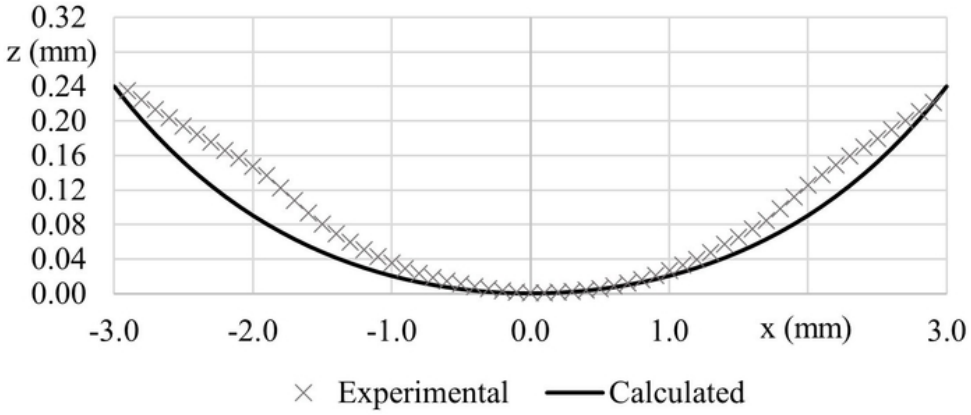

121x53mm (150 x 150 DPI)

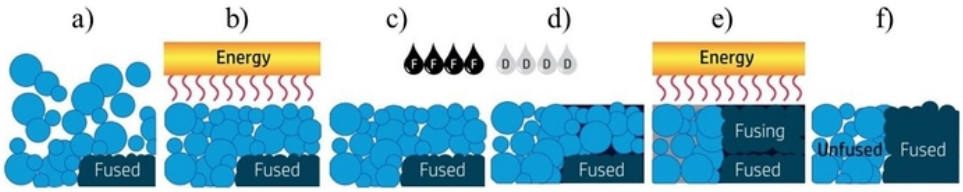

121x23mm (150 x 150 DPI)

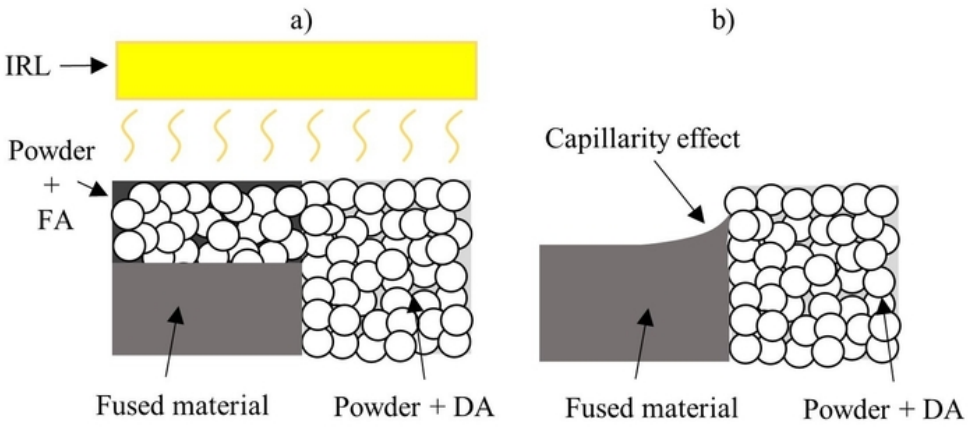

121x52mm (150 x 150 DPI)

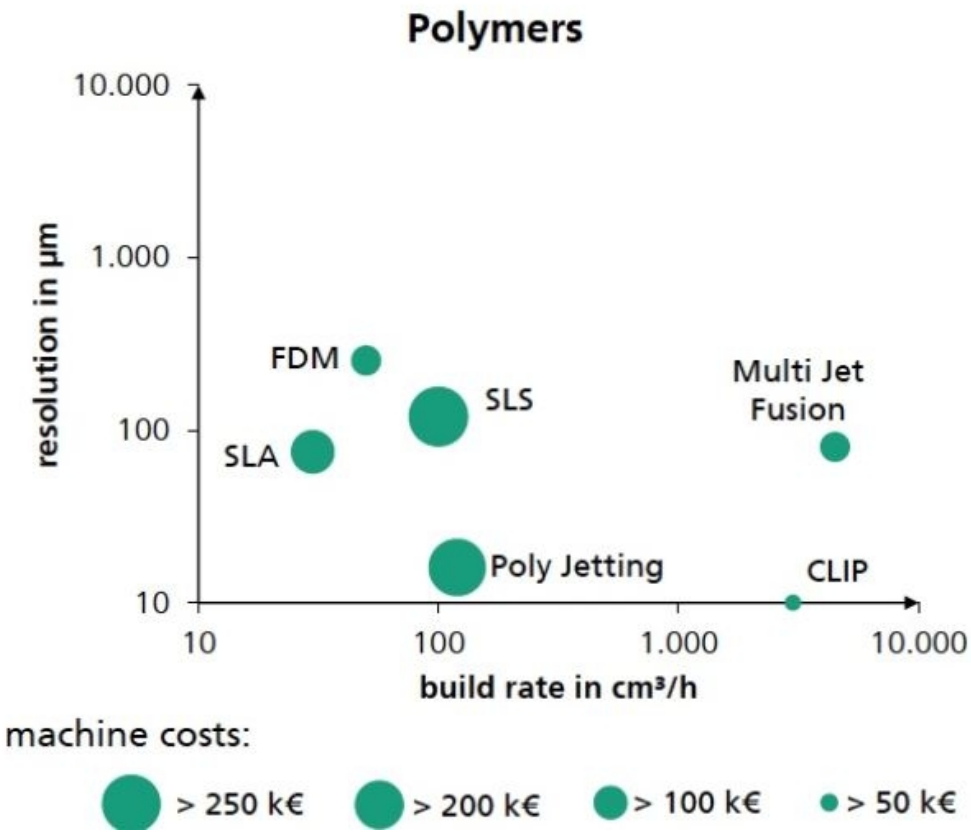

160x137mm (96 x 96 DPI)

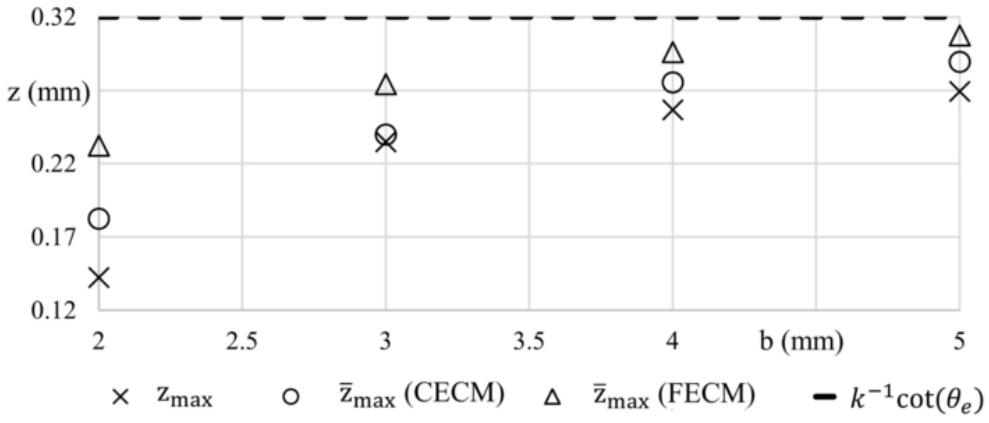

121x53mm (150 x 150 DPI)